Available online at www.sciencedirect.com
ScienceDirect
International Journal of Heat and Mass Transfer 51 (2008) 5024–5032
International Journal of HEAT and MASS TRANSFER
www.elsevier.com/locate/ijhmt

Technical Note

Natural convection in a vertical annulus driven by a central heat generating rod

P. Venkata Reddy [a], G.S.V.L. Narasimham [b,*]

[a] CFD Center, Department of Aerospace Engineering, Indian Institute of Science, Bangalore 560012, India
[b] Department of Mechanical Engineering, Indian Institute of Science, Bangalore 560012, India

Received 20 September 2007; received in revised form 4 January 2008
Available online 16 April 2008

Abstract

A numerical study of the conjugate natural convection in a vertical annulus with a centrally located vertical heat generating rod is performed. The formulation in primitive form is solved using a pressure-correction algorithm. A parametric study is conducted by varying the heat generation based Grashof number, aspect ratio and the solid-to-fluid thermal conductivity ratio over wide ranges with the Prandtl number fixed at 0.7. Results are presented for the temperature distributions and Nusselt numbers. The average Nusselt numbers on the inner and outer boundaries show an increasing trend with the Grashof number. Correlations are presented for the Nusselt number and the dimensionless temperatures of interest in terms of the parameters of the problem.

Keywords: Conjugate natural convection; Heat generation; Vertical annulus

1. Introduction

Natural convection heat transfer in a differentially heated vertical annulus was investigated both experimentally and numerically by several investigators. In these studies, the heat transfer in the annulus is delineated into three flow regimes, viz., conduction, transition and boundary-layer regimes. Beginning from the studies reported in [1,2], natural convection in vertical annuli with isothermal warm inner and cold outer vertical surfaces received much attention [3–7], where a thorough coverage of the literature can be found. The case of a vertical annulus with isoflux inner vertical surface and isothermal outer vertical surface was considered in [5,8]. The coupling of conduction and natural convection in a vertical annulus was studied in [9,10]. The present work is a numerical study of the conjugate natural convection heat transfer in a vertical annulus. The convection is driven by the volumetric heat generation in a centrally placed solid circular rod. The problem finds applications in spent nuclear casks and electrical and electronic equipment, where, apart from the natural convection taking place in the annulus, the temperature distribution in the central vertical rod is of interest. This necessitates the solution of a conjugate problem. For instance, spent nuclear fuel casks contain one or more canisters of circular, square or hexagonal cross-section, containing bundles of fuel rods arranged in triangular or square arrays. The canister can often be modelled as a heat generating solid with an equivalent thermal conductivity, as the natural convection in the fill gas is often negligible. Methods of calculating equivalent thermal conductivity of such arrays of tubes or rods have been presented in [11]. The quantities of interest in the present study are the maximum and average temperatures of the rod, local heat flux and Nusselt number distributions on the inner and outer surfaces of the annulus, the flow and temperature distributions and the average Nusselt numbers.

2. Governing equations and solution method

Fig. 1 shows the physical model and the coordinate system. The cylindrical polar coordinate system is chosen to

* Corresponding author. Tel.: +91 80 22932971; fax: +91 80 23600648.
E-mail address: mecgsvln@mecheng.iisc.ernet.in (G.S.V.L. Narasimham).

0017-9310/$ - see front matter © 2008 Elsevier Ltd. All rights reserved.
doi:10.1016/j.ijheatmasstransfer.2008.02.032

Nomenclature

a	thermal diffusivity, $m^2\ s^{-1}$
c_p	specific heat at constant pressure, $J\ kg^{-1}\ K^{-1}$
g	acceleration due to gravity, $m\ s^{-2}$
Gr	Grashof number, $g\beta\Delta T_c L_c^3/\nu_c^2$, dimensionless
L_c	characteristic dimension (annulus gap width), $R_o - R_i$, m
H	height of the annulus, m
Nu	Nusselt number, $\alpha L_c/\lambda_c$, dimensionless
p	excess pressure over the hydrostatic, Pa
Pr	Prandtl number, $\eta c_p/\lambda_c$, dimensionless
$\dot{Q}_{v,c}$	characteristic volumetric heat generation rate, $W\ m^{-3}$
R_i	inner radius of the annulus, m
R_o	outer radius of the annulus, m
t	time, s
T	temperature, K
v_r, v_z	velocities in the r and z directions, $m\ s^{-1}$
r, z	cylindrical coordinates, m

Greek symbols

α	heat transfer coefficient, $W\ m^{-2}\ K^{-1}$
β	volumetric expansion coefficient, K^{-1}
ΔT_c	characteristic temperature difference, $\dot{Q}_{v,c}L_c^2/\lambda_c$, K
η	dynamic viscosity, Pa s
κ	radius ratio, R_o/R_i, dimensionless
λ	thermal conductivity, $W\ m^{-1}\ K^{-1}$
ν	kinematic viscosity, $m^2\ s^{-1}$
ρ	density, $kg\ m^{-3}$
ψ	stream function, $\psi_{ref} + \int r(v_z dr - v_r dz)$, $m^3\ s^{-1}$

Subscripts

av	average
i	inner boundary
l	local
o	outer boundary
ref	reference
s	solid
cl	centreline
max	maximum

Superscript

*	dimensionless quantity

describe the geometry, with the origin placed at the centre of the bottom plate. Assuming axi-symmetry, a semi-vertical r–z plane marked OABCDEO is considered for the analysis. The top and bottom end plates are adiabatic. The flow equations are written subject to the Boussinésq approximation [12]. The temperature differences are assumed to be sufficiently small in order to neglect the radiation heat transfer. The continuity, radial momentum, axial momentum and energy equations in dimensionless form are, respectively, as follows:

$$\frac{1}{r^*}\frac{\partial}{\partial r^*}(\rho^* r^* v_r^*) + \frac{\partial}{\partial z^*}(\rho^* v_z^*) = 0 \tag{1}$$

$$\frac{\partial}{\partial t^*}(\rho^* v_r^*) + \frac{1}{r^*}\frac{\partial}{\partial r^*}(\rho^* r^* v_r^* v_r^*) + \frac{\partial}{\partial z^*}(\rho v_z^* v_r^*) = \frac{1}{r^*}\frac{\partial}{\partial r^*}\left(r^*\eta^*\frac{\partial v_r^*}{\partial r^*}\right) + \frac{\partial}{\partial z^*}\left(\eta^*\frac{\partial v_r^*}{\partial z^*}\right) + S_{vr}^* \tag{2}$$

$$\frac{\partial}{\partial t^*}(\rho^* v_z^*) + \frac{1}{r^*}\frac{\partial}{\partial r^*}(\rho^* r^* v_r^* v_z^*) + \frac{\partial}{\partial z^*}(\rho v_z^* v_z^*) = \frac{1}{r^*}\frac{\partial}{\partial r^*}\left(r^*\eta^*\frac{\partial v_z^*}{\partial r^*}\right) + \frac{\partial}{\partial z^*}\left(\eta^*\frac{\partial v_z^*}{\partial z^*}\right) + S_{vz}^* \tag{3}$$

$$\frac{\partial}{\partial t^*}(\rho^* T^*) + \frac{1}{r^*}\frac{\partial}{\partial r^*}(\rho^* r^* v_r^* T^*) + \frac{\partial}{\partial z^*}(\rho^* v_z^* T^*) = \frac{1}{r^*}\frac{\partial}{\partial r^*}\left(r^*\frac{\lambda^*}{Prc_p^*}\frac{\partial T^*}{\partial r^*}\right) + \frac{\partial}{\partial z^*}\left(\frac{\lambda^*}{Prc_p^*}\frac{\partial T^*}{\partial z^*}\right) + S_T^* \tag{4}$$

where the source terms appearing in the above equations are

$$S_{vr}^* = \frac{\partial}{\partial z^*}\left(\eta^*\frac{\partial v_z^*}{\partial r^*}\right) + \frac{1}{r^*}\frac{\partial}{\partial r^*}\left(r^*\eta^*\frac{\partial v_r^*}{\partial r^*}\right) + \frac{2\eta^*}{r^{*2}}v_r^* - \frac{\partial p^*}{\partial r^*} \tag{5}$$

$$S_{vz}^* = \frac{\partial}{\partial z^*}\left(\eta^*\frac{\partial v_z^*}{\partial z^*}\right) + \frac{1}{r^*}\frac{\partial}{\partial r^*}\left(r^*\eta^*\frac{\partial v_r^*}{\partial z^*}\right) - \frac{\partial p^*}{\partial z^*} + \rho^*\beta^* GrT^* \tag{6}$$

$$S_T^* = \frac{\dot{Q}_v^*(r^*, z^*)}{Prc_p^*} \tag{7}$$

The dimensionless quantities appearing in the above equations are defined as

$$t^* = \frac{t v_c}{L_c^2}, \quad r^* = \frac{r}{L_c}, \quad z^* = \frac{z}{L_c}$$
$$v_r^* = \frac{v_r}{v_c/L_c}, \quad v_z^* = \frac{v_z}{v_c/L_c}, \quad p^* = \frac{p}{\rho_c(v_c/L_c)^2}$$
$$T^* = \frac{T - T_c}{\Delta T_c}, \quad \Delta T_c = \frac{\dot{Q}_{v,c}L_c^2}{\lambda_c} \tag{8}$$
$$\rho^* = \frac{\rho}{\rho_c}, \quad c_p^* = \frac{c_p}{c_{p,c}}, \quad \eta^* = \frac{\eta}{\eta_c}, \quad \lambda^* = \frac{\lambda}{\lambda_c}, \quad \beta^* = \frac{\beta}{\beta_c}$$
$$\dot{Q}_v^*(r^*, z^*) = \frac{\dot{Q}_v(r, z)}{\dot{Q}_{v,c}}, \quad Gr = \frac{g\beta_c\Delta T_c L_c^3}{\nu_c^2}, \quad Pr = \frac{\nu_c}{a_c}$$

In the above system of non-dimensionalization, the subscript c denotes the characteristic or reference quantity. The characteristic dimension L_c is the gap width $R_o - R_i$. The reference temperature T_c is the same as the annulus outer boundary temperature T_o. The quantity $\dot{Q}_v^*(r^*, z^*)$

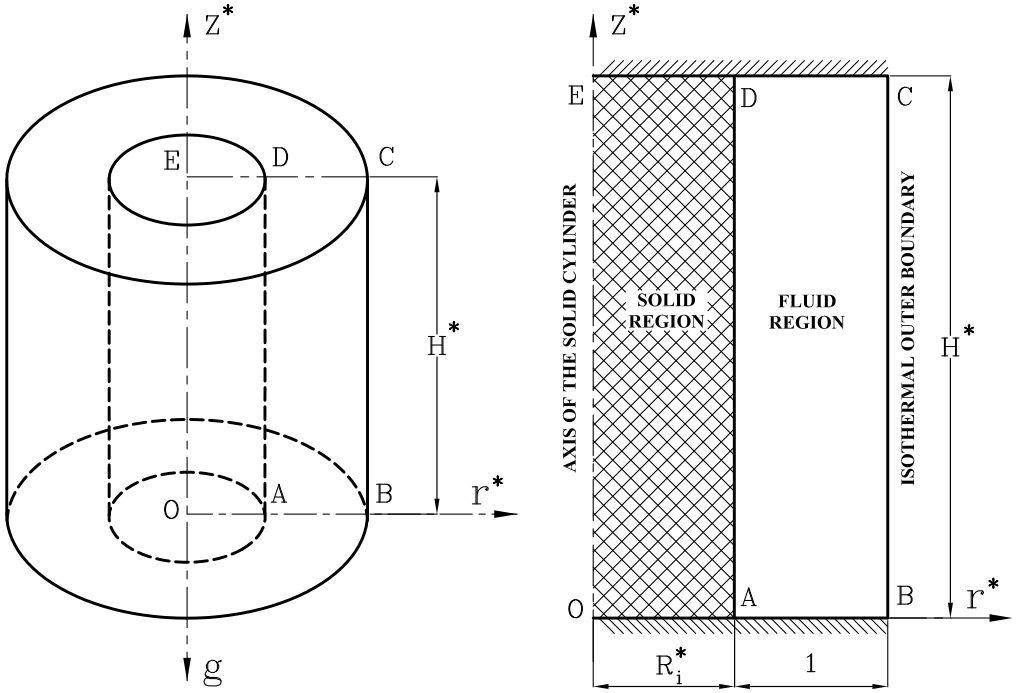

Fig. 1. Physical model and coordinate system.

in Eq. (7) is set to unity in the solid and to zero in the fluid. Eq. (4) applies to fluid region with the source term set to zero. The same equation applies to the concentrically placed vertical solid cylinder with the velocities set to zero. The characteristic properties correspond to those of the fluid and hence the dimensionless property ratios mentioned in Eq. (7) take a value of unity in the fluid region and appropriate values, denoted here as ρ_s^*, c_s^* and λ_s^*, in the solid. Steady state results are obtained as long-time solutions of the time-dependent equations. The solid region is considered as a fluid region of infinite viscosity by setting the quantity η_s^* to a very large number. The quantity β^* is set to unity in the fluid region and to zero in the solid region. In the steady state, since the time derivatives of the dependent variables vanish, the actual value of the solid thermal capacitance $\rho_s^* c_s^*$ is immaterial. In view of this, ρ_s^* and c_s^* are set to unity in the present numerical formulation. Thus the time marching solution for the solid energy equation may be considered as a false transient.

The initial conditions are zero dimensionless velocities in the fluid region and zero dimensionless temperature throughout the computational domain. The hydrodynamic boundary conditions are no-slip and zero permeability on all solid boundaries. The thermal boundary conditions are zero dimensionless temperature on the outer surface of the annulus, adiabatic conditions on the top and bottom surfaces and zero temperature gradient condition on the centreline of the rod. At the interface between the rod and the fluid, heat flux continuity and no temperature jump conditions are assumed.

The parameters of the problem are the dimensionless inner radius R_i^* of the annulus, the aspect ratio H^*, the heat generation based Grashof number Gr, the Prandtl number Pr of the fluid and the solid-to-fluid thermal conductivity ratio λ_s^*. The radius ratio $\kappa(= R_o^*/R_i^* = 1 + 1/R_i^*)$ can be employed as an alternative parameter to the dimensionless inner radius R_i^*. The local and the average heat transfer coefficients are based on the difference between the average interface temperature and the outer boundary temperature. The local Nusselt number on the inner surface is given by

$$Nu_{l,i} = -\frac{1}{T^*_{av,i}}\left[\frac{\partial T^*}{\partial r^*}\right]_{l,i} \tag{9}$$

The average Nusselt number on the inner surface can be obtained by integration of the local Nusselt number. The Nusselt numbers for the outer boundary are similarly defined. The total heat transfer rate through both the inner and outer boundaries should equal the heat generation rate. Therefore the relation connecting the inner and outer surface average Nusselt numbers is

$$Nu_{av,i} T^*_{av,i} 2\pi R_i^* H^* = Nu_{av,o} T^*_{av,i} 2\pi R_o^* H^* = \pi R_i^{*2} H^* \tag{10}$$

The governing equations are discretised on a staggered mesh [13]. The SIMPLEC algorithm [14] is employed for the pressure–velocity coupling. In generating the mesh in each direction, the coordinates corresponding to the control volume faces are first calculated and the pressure nodes are placed at the geometric centres of the control volumes. The Roberts transformation [15] is used for mesh generation in each direction. The time derivatives are approximated by backward differences and the diffusive terms, by central differences. The convective terms are discretised with a third-order accurate, hybrid linear and parabolic approximation [16]. For velocity corrections, the velocity nodes belonging to the fluid and solid regions are

identified. For the fluid region nodes, the velocity corrections are implemented in the usual manner, while for the solid region, the velocity corrections are set to zero in order that the velocities remain at the initially prescribed zero values. The discretised equations are solved with the modified strongly implicit procedure (MSIP) [17]. The time step employed is typically 25 times of that allowable by an explicit method [18] and depends on the parameter set. A sequential solution scheme is adopted by first solving the momentum and the pressure correction equations, and correcting the velocities and the pressure. Next, the energy equation is solved. Global iterations are continued over the same time step until the required coupling between the equations is achieved. The time marching is continued until satisfactory time convergence is achieved.

Table 1
Comparison of the present Nusselt numbers with those of Farouk, Ball and Dixit (FBD) [3] for the differentially heated annulus for $Gr = 10^5$ and $\kappa = 2$

H^*	$Pr = 0.07$			$Pr = 0.7$			$Pr = 7.0$		
	FBD	PR	PD	FBD	PR	PD	FBD	PR	PD
0.5	1.10	1.09	0.91	3.10	2.88	7.10	7.70	7.65	0.65
1.0	1.75	1.71	2.29	3.50	3.74	6.86	8.10	7.70	4.94
5.0	1.50	1.51	0.67	3.15	3.14	0.32	5.70	5.85	2.63

PR = present results, PD = percentage difference.

Following a grid sensitivity study, the radial mesh spacings are chosen between $10 + 25$ (i.e., 10 in the solid and 25 in the fluid) and $25 + 25$ depending upon the radius ratio and the axial spacings are chosen between 50 and 125, depending upon the aspect ratio. The criterion used for time convergence is the attainment of energy balance to within 5% as well as a relative change of less than 10^{-6} in the maximum temperature over one hundred time steps (for instance, at $Gr = 10^8$, the time step ranged from 6.5×10^{-5} to 6.5×10^{-4}). At each time step, a relative change of 10^{-5} in the maximum temperature between successive iterations is used to terminate the global iterative process with the maximum global iterations fixed between three and five. The computer program is validated by comparing the equivalent conductivity values obtained from the present code with those reported in Farouk et al. [3], for a differentially heated annulus. The comparison is shown in Table 1 for various aspect ratios and Prandtl numbers for a Grashof number (based on $T_o - T_i$) of 10^5 and radius ratio 2. As can be seen from this Table, there is a good agreement between the two sets of results.

3. Results and discussion

Results are obtained for a wide parametric space, the ranges of the parameters being 10^6–10^{10} for Grashof number (Gr), 1–15 for aspect ratio (H^*), 2–8 for radius ratio (κ)

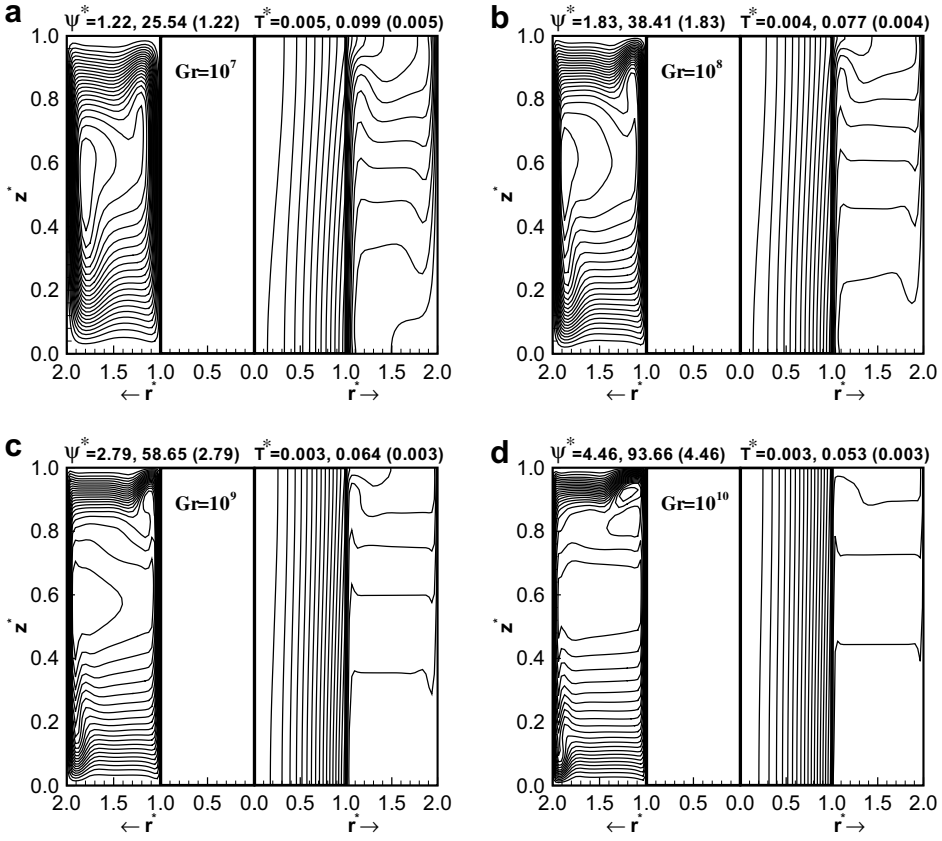

Fig. 2. Streamlines and isotherms for $H^* = 1$, $\kappa = 2$ and $\lambda_s^* = 5$.

and 5–100 for solid-to-fluid thermal conductivity ratio (λ_s^*). As can be seen from the results, the heat generation based Grashof number Gr is generally two to three orders of magnitude higher than the temperature difference based Grashof number. In view of this, steady laminar flow solutions could be obtained for Gr values as high as 10^{10}. The working medium is air for which the Prandtl number is taken as 0.7.

3.1. Streamline and isotherm maps

Selected streamline and isotherm maps are shown in Figs. 2–5. Fig. 2 corresponds to thermal conductivity ratio 5, aspect ratio 1 and radius ratio 2 and Grashof numbers 10^7, 10^8, 10^9 and 10^{10}. The isotherm maps in Fig. 2 show that the dimensionless temperatures decrease as the Grashof number increases. This means that, as the Grashof number increases, the temperature difference $T - T_o$ increases at a slower rate than the heat generation based characteristic temperature difference ΔT_c. The isotherm maps show that the core region of the annulus tends to become stratified. The stratification effect increases as the Grashof number increases. The slightly slanting isotherms in the heat generating solid cylinder show that the temperature distribution in the solid is mostly radial. Large radial temperature gradients can also be seen in the fluid near the solid–fluid interface. The fluid circulation inside the annulus at lower Grashof numbers is characterised by an elongated uni-cellular motion, with a stagnation point occurring near the central part of the outer boundary. The stream function values show that the circulation inside the annulus intensifies as the Grashof number increases and that the stagnation point tends to move horizontally towards the inner boundary. In addition, eddies tend to develop at the top end of the inner boundary. The effect of the aspect ratio on the flow and temperature distributions can be seen by comparing Fig. 2a with Fig. 3a and b. The isotherms in the solid slant more with increasing aspect ratio indicating that significant axial temperature gradients can occur in the solid apart from the radial temperature gradients. Higher aspect ratios increase the temperatures in the system due to higher heat generation rates and increase the strength of the circulation inside the annulus. Higher aspect ratios increase the temperature stratification in the upper part of the annulus, while lessening the same in the lower part and also promote the tendency for the formation of recirculation zones in the upper part of the annulus. When the radius ratio is increased, the temperatures as well as the stream function values decrease owing to the decreased total heat generation, as is revealed by a comparison of Fig. 2a with Fig. 4a and b. Moreover, the two-dimensionality of the solid temperature distribution becomes more prominent. Figs. 2a, 5a and b show that increasing solid-to-fluid

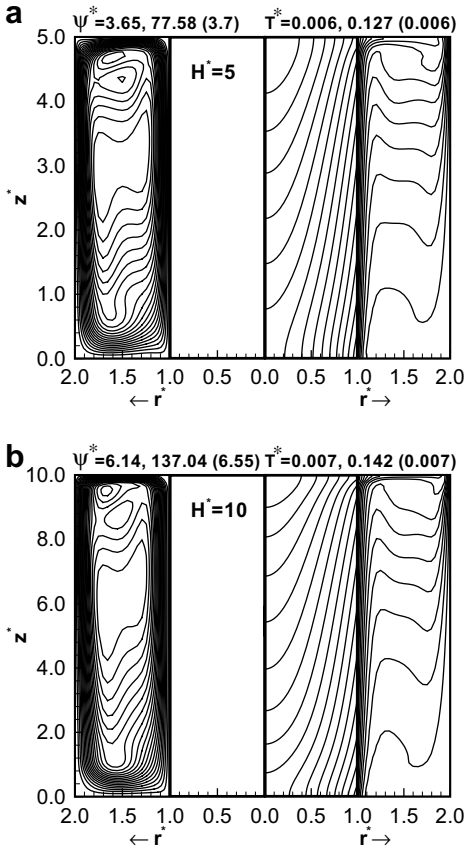

Fig. 3. Streamlines and isotherms for $Gr = 10^7$, $\kappa = 2$ and $\lambda_s^* = 5$.

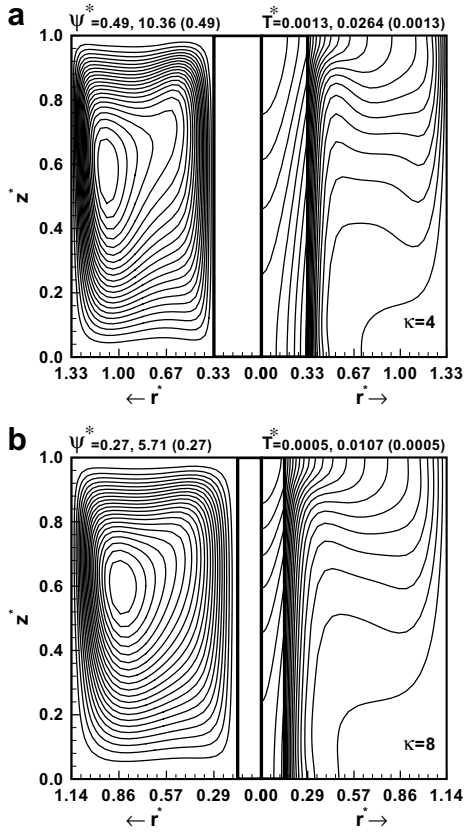

Fig. 4. Streamlines and isotherms for $Gr = 10^7$, $H^* = 1$ and $\lambda_s^* = 5$.

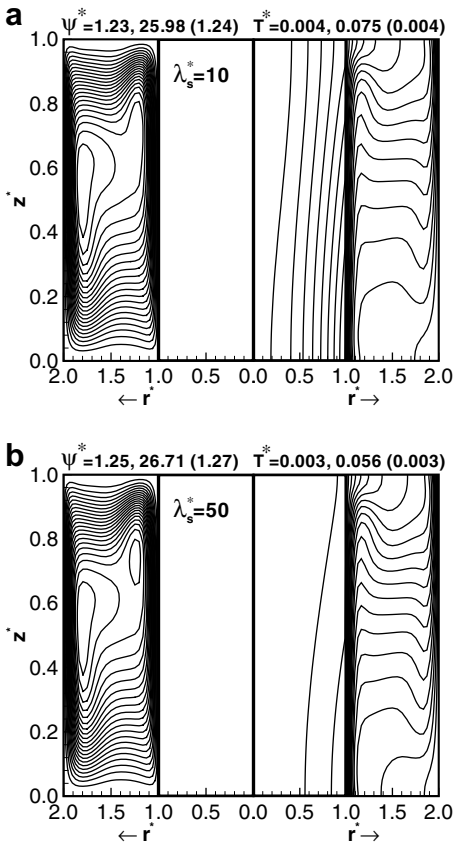

Fig. 5. Streamlines and isotherms for $Gr = 10^7$, $H^* = 1$ and $\kappa = 2$.

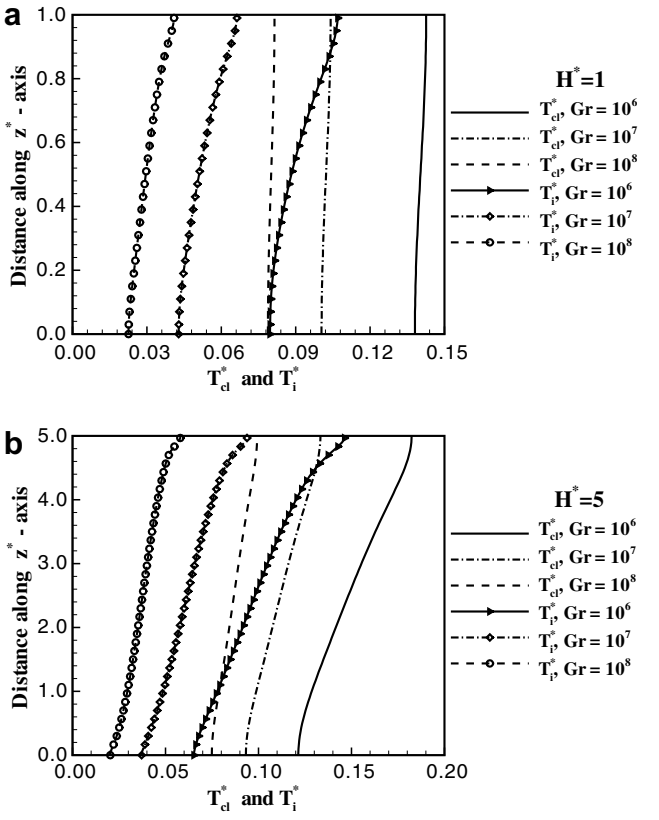

Fig. 6. Axial variation of the centreline and the interface temperatures for $\lambda_s^* = 5$ and $\kappa = 2$.

thermal conductivity ratio has the effect of homogenising the temperature in the solid and consequently resulting in a reduction in the radial and axial temperature gradients in the solid. However, there occur only minor changes in the circulation and temperature distribution inside the annulus.

3.2. Axial temperature variation on the rod axis and the interface

Fig. 6 presents the dimensionless temperature variation in the axial direction along the axis of the rod and along the interface for $\lambda_s^* = 5$, $\kappa = 2$, $H^* = 1$ and 5, and Grashof numbers 10^6, 10^7 and 10^8. It can be seen that at a given thermal conductivity ratio, the temperatures on the rod axis and the interface increase in the axial direction with the effect much more pronounced for lower Grashof numbers than for higher Grashof numbers. The maximum temperatures always occur in the solid at the top end of the annulus.

3.3. Axial variation of local Nusselt numbers on the inner and outer boundaries of the annulus

Fig. 7 shows the variation of local Nusselt numbers in the axial direction along the inner and outer boundaries. The results are presented for the cases of $\lambda_s^* = 5$, $\kappa = 2$, $H^* = 1$ and 5 and Grashof numbers 10^6, 10^7 and 10^8. As can be seen from Fig. 7, there is a considerable axial variation of the Nusselt number on the inner boundary at lower aspect ratios. Fig. 7 also shows that for these parameter values, there is not much axial variation in the local Nusselt number on the inner boundary. The variation of the Nusselt number along the outer boundary shows that the maximum value occurs at the top and decreases towards the bottom wall.

3.4. Variation of average solid, average inner boundary and maximum temperatures with Grashof number

Fig. 8 shows the variation of average solid temperature, maximum solid temperature and the average temperature of the interface with respect to the Grashof number for aspect ratios 1 and 5. The values of the thermal conductivity ratio and the radius ratio are 5 and 2, respectively. The maximum dimensionless temperature in the solid decreases as the Grashof number increases. A similar trend can be observed for the dimensionless average temperature of the solid and the dimensionless average interface temperature. As the aspect ratio increases, qualitatively similar trends can be seen. In view of the definition of the dimensionless temperature, although the values of T^* show a decreasing trend, the dimensional temperatures actually increase with volumetric heat generation rate. This is

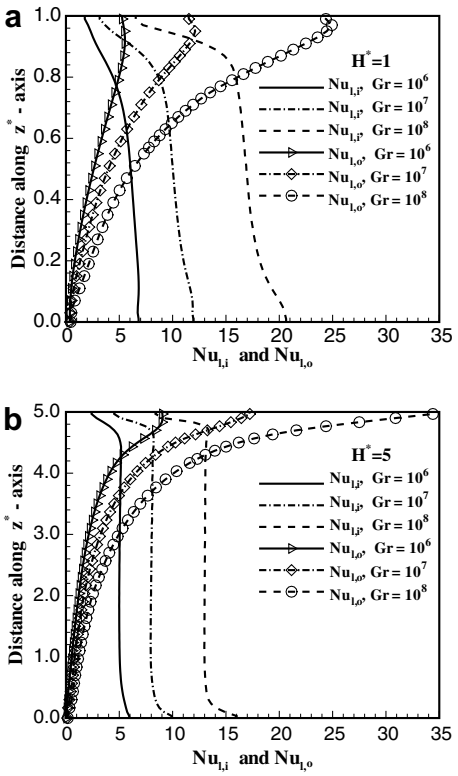

Fig. 7. Axial variation of the Nusselt numbers on inner and outer boundaries for $\lambda_s^* = 5$ and $\kappa = 2$.

shown in Fig. 9 for $\kappa = 2$, $\lambda_s^* = 5$, $H^* = 1$, $R_o = 0.5$ and $T_o = 40$ °C.

3.5. Average Nusselt numbers on the inner and outer boundaries

Fig. 10 shows the variation of the average Nusselt numbers for the inner and outer boundaries with respect to the Grashof number for the same parameter values mentioned in Section 3.4. The average Nusselt numbers on the inner and outer boundaries $Nu_{av,i}$ and $Nu_{av,o}$ show an increasing trend with Grashof number. It can be seen that the inner boundary Nusselt number is greater than that of the outer boundary at any Gr. Moreover, the rate of increase of the

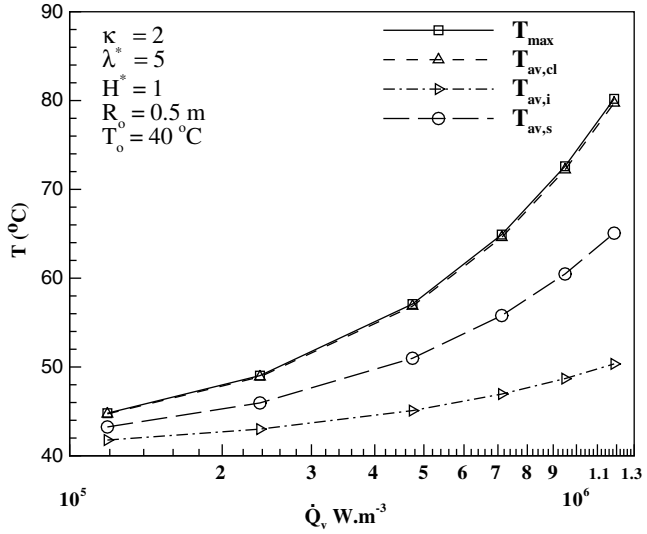

Fig. 9. Variation of dimensional temperatures with volumetric heat generation rate for $\kappa = 2$, $\lambda_s^* = 5$, $H^* = 1$, $R_o = 0.5$ and $T_o = 40$ °C.

average Nusselt number is higher at higher Grashof numbers. The results have also revealed that the average Nusselt number predicted by the conjugate analysis generally lies between the Nusselt numbers of the equivalent isothermal and isoflux cases, the isothermal Nusselt numbers being the lowest. The average Nusselt numbers of the conjugate analysis are found to be comparable to those of the equivalent isoflux case at aspect ratios ranging from 1 to 5 and for low to moderate conductivity ratios.

3.6. Correlations

Correlations are obtained for the dimensionless maximum temperature T^*_{max}, average centreline temperature $T^*_{av,cl}$, average inner surface temperature $T^*_{av,i}$, average solid temperature $T^*_{av,s}$ and the average Nusselt number $Nu_{av,i}$, in the form $aGr^bH^{*c}\kappa^{(d+e/\kappa)}[1 + g\exp(-\lambda_s^*)]^f$, for each quantity. The constants a–f are obtained by subjecting the computed data to a multiple non-linear regression analysis. The correlation constants are presented in Table 2.

In Table 2, e_s is the standard error of estimate and R^2 is the multiple correlation. In the functional form, the exponent on the radius ratio is chosen as a function of radius

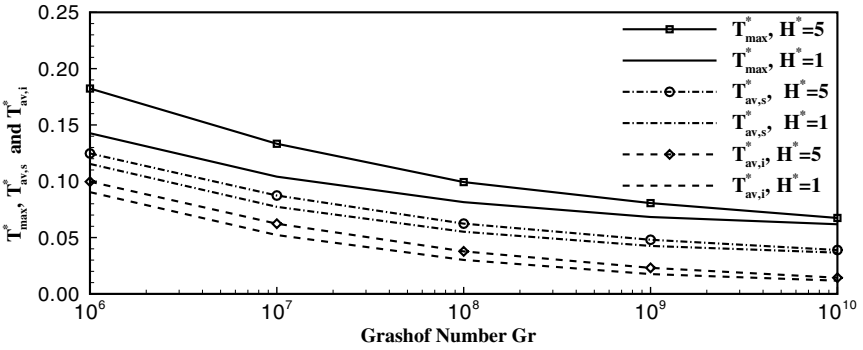

Fig. 8. Variation of T^*_{max}, $T^*_{av,s}$ and $T^*_{av,i}$ with Grashof number for $\lambda_s^* = 5$ and $\kappa = 2$.

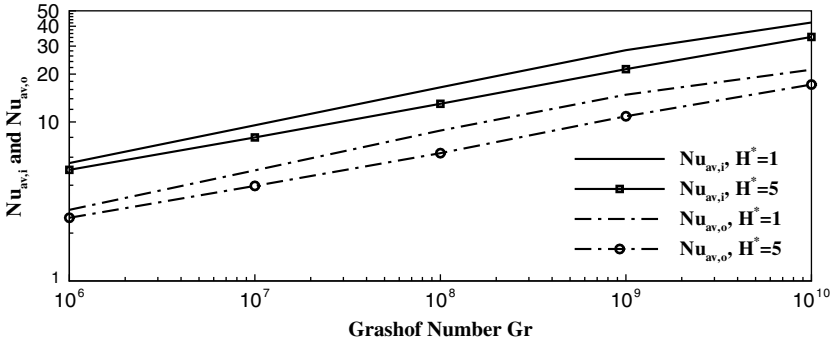

Fig. 10. Variation of $Nu_{av,i}$ and $Nu_{av,o}$ with Grashof number for $\lambda^*_s = 5$ and $\kappa = 2$.

Table 2
Correlation constants

Constant	Quantity				
	T^*_{max}	$T^*_{av,cl}$	$T^*_{av,i}$	$T^*_{av,s}$	$Nu_{av,i}$
a	12.8875	14.2733	7.7668	11.5426	0.5248
b	−0.1722	−0.1677	−0.2013	−0.1804	0.2001
c	0.1849	0.1075	0.1335	0.1168	−0.1360
d	−1.7501	−1.8402	−1.4872	−1.7095	−0.1139
e	−3.5265	−3.9636	−2.1839	−3.3630	−0.6193
f	1.0543	1.2120	−1.4621	1.1973	1.7136
g	57.5526	48.3747	1.0315	27.9250	1.1357
e_s	0.0271	0.0311	0.0034	0.0139	0.0037
R^2	0.9883	0.9868	0.9984	0.9937	0.9959

ratio itself following the suggestion of Khan and Kumar [8]. The form of the term containing the thermal conductivity ratio is suggested by the fact that as the thermal conductivity ratio increases, the solid becomes more and more isothermal and the temperatures tend to attain constant values. The average Nusselt number at the outer boundary $Nu_{av,o}$ is related to the average Nusselt number at the inner boundary $Nu_{av,i}$ through the relation $Nu_{av,o} = (R^*_i/R^*_o)Nu_{av,i} = \kappa Nu_{av,i}$. Thus, the Nusselt number at the outer boundary can be computed using the Nusselt number at the inner boundary and the radius ratio.

4. Conclusions

A numerical study of natural convection in a vertical annulus with isothermally cooled outer boundary and driven by a centrally located heat generating solid cylinder is performed. In the parameter range considered, the flow in the annulus is unicellular except at higher aspect ratios, at which additional eddies can occur in the upper part of the fluid region in the annulus. The core region of the annulus exhibits temperature stratification. Higher aspect ratios promote two-dimensionality in the solid temperature distribution. The average Nusselt number from the conjugate analysis lies between the Nusselt numbers of the isothermal and the isoflux cases, the isothermal Nusselt numbers being the lowest. It is possible to approximate the annulus convection in the conjugate case with that of the isoflux case at aspect ratios 1–5 and for low to moderate conductivity ratios, provided the solid temperature distribution is not of interest. At higher aspect ratios, the coupling between the conduction and convection becomes important. Higher solid-to-fluid thermal conductivity ratio homogenises the temperature in the solid and reduces the radial and axial temperature gradients in the solid without causing any major changes in the circulation and temperature distribution inside the annulus. The increase of centreline and interface temperatures in the axial direction is more pronounced for lower Grashof numbers. The average inner and outer wall Nusselt numbers are found to increase with Grashof number, while the opposite is true in respect of average solid, average inner boundary and the maximum temperature. Correlations are obtained for estimating the Nusselt numbers and the temperatures of interest.

References

[1] G. de Vahl Davis, R.W. Thomas, Natural convection between concentric vertical cylinders, high speed computing in fluid dynamics, Phys. Fluids 12 (1969) 198–207.
[2] R.W. Thomas, G. de Vahl Davis, Natural convection in annular and rectangular cavities–a numerical study, in: Proceedings of the Fourth International Heat Transfer Conference, vol. 4, 1970, Paper NC 2.4.
[3] B. Farouk, K.S. Ball, V.C. Dixit, Aspect and radius ratio effects on natural convection in a vertical annulus, in: Proceedings of the 9th International Heat Transfer Conference, vol. 2, 1990, pp. 585–590.
[4] E.K. Glakpe, C.B. Watkins Jr., B. Kurien, Solution of three-dimensional natural convection about a vertical square rod in a cylindrical enclosure, Int. J. Numer. Meth. Fluids 7 (1987) 155–173.
[5] M. Keyhani, F.A. Kulacki, R.N. Christensen, Free convection in a vertical annulus with constant heat flux on the inner wall, Trans. ASME, J. Heat Transfer 105 (1983) 454–459.
[6] R. Kumar, M.A. Kalam, Laminar thermal convection between vertical coaxial isothermal cylinders, Int. J. Heat Mass Transfer 34 (1991) 513–524.
[7] V. Prasad, F.A. Kulacki, Free convective heat transfer in a liquid-filled vertical annulus, Trans. ASME, J. Heat Transfer 107 (1985) 596–602.
[8] J.A. Khan, R. Kumar, Natural convection in vertical annuli: a numerical study for constant heat flux on the inner wall, Trans. ASME, J. Heat Transfer 111 (1989) 909–915.
[9] M.J. Fishbaugher, D. Kim, Natural convection in a vertical annulus with a cocentric baffle, in: ASME Proceedings of the 1988 National Heat Transfer Conference, HTD-96, Texas, vol. 3, 1988, pp. 273–279.
[10] K. Choukairy, R. Bennacer, P. Vasseur, Natural convection in a vertical annulus boarded by an inner wall of finite thickness, Int. Commun. Heat Mass Transfer 31 (2004) 501–512.

[11] R.D. Manteufel, N.E. Todreas, Analytic formulae for the effective conductivity of a square or hexagonal array of parallel tubes, Int. J. Heat Mass Transfer 31 (1994) 647–657.
[12] D.D. Gray, A. Giorgini, The validity of Boussinesq approximation for liquid and gases, Int. J. Heat Mass Transfer 19 (1976) 543–551.
[13] S.V. Patankar, Numerical heat transfer and fluid flow, in: W.J. Minkowycz, E.M. Sparrow (Eds.), Series in Computational Methods in Mechanics and Thermal Sciences, Hemisphere Publishing Corporation/McGraw-Hill Book Company, Washington/New York, 1980.
[14] J.P. Van Doormaal, G.D. Raithby, Enhancements of the SIMPLE method for predicting incompressible fluid flows, Numer. Heat Transfer 7 (1984) 147–163.
[15] G.O. Roberts, Computational meshes for boundary layer problems, in: M. Holt (Ed.), Proceedings of the Second International Conference on Numerical Methods in Fluid Dynamics, Springer-Verlag, Berlin, 1971, pp. 171–177.
[16] J. Zhu, A low-diffusive and oscillation-free convection scheme, Commun. Appl. Numer. Meth. 7 (1991) 225–232.
[17] G.E. Schneider, M. Zedan, A modified strongly implicit procedure for the numerical solution of field problems, Numer. Heat Transfer 4 (1981) 1–19.
[18] J.D. Hellums, S.W. Churchill, Computation of natural convection by finite difference methods, Int. Dev. Heat Transfer, ASME (1963) 985–993.